Topologically Localized Vibronic Excitations in Second-Layer Graphene Nanoribbons

Zhengya Wang,[1] Ruoting Yin,[1] Zixi Tang,[1] Hongjian Du,[1,2] Yifan Liang,[1,2] Xiaoqing Wang,[1,2] Qing-Song Deng,[3] Yuan-Zhi Tan,[3] Yao Zhang,[1,2] Chuanxu Ma,[1,2,*] Shijing Tan,[1,2] and Bing Wang[1,2,†]

[1]*Hefei National Research Center for Physical Sciences at the Microscale and Synergetic Innovation Center of Quantum Information and Quantum Physics, and New Cornerstone Science Laboratory, University of Science and Technology of China, Hefei, Anhui 230026, China*

[2]*Hefei National Laboratory, University of Science and Technology of China, Hefei 230088, China*

[3]*Collaborative Innovation Center of Chemistry for Energy Materials, State Key Laboratory for Physical Chemistry of Solid Surfaces, and Department of Chemistry, College of Chemistry and Chemical Engineering, Xiamen University, 361005 Xiamen, China*

(Received 10 December 2023; accepted 6 June 2024; published 15 July 2024)

It is of fundamental importance to characterize the intrinsic properties, like the topological end states, in the on-surface synthesized graphene nanoribbons (GNRs), but the strong electronic interaction with the metal substrate usually smears out their characteristic features. Here, we report our approach to investigate the vibronic excitations of the topological end states in self-decoupled second-layer GNRs, which are grown using an on-surface squeezing-induced spillover strategy. The vibronic progressions show highly spatially localized distributions at the second-layer GNR ends, which can be ascribed to the decoupling-extended lifetime of charging through resonant electron tunneling at the topological end states. In combination with theoretical calculations, we assign the vibronic progressions to specific vibrational modes that mediate the vibronic excitations. The spatial distribution of each resolved excitation shows evident characteristics beyond the conventional Franck-Condon picture. Our work by direct growth of second-layer GNRs provides an effective way to explore the interplay between the intrinsic electronic, vibrational, and topological properties.

DOI: 10.1103/PhysRevLett.133.036401

Bottom-up synthesized atomically precise graphene nanoribbons (GNRs) [1–3] represent an emerging class of designer quantum materials that can host tunable electronic structures [4,5], topological interface or end states [6–11], and magnetic spin centers [12–15], which have attracted enormous interest in nanoelectronics, optoelectronics, spintronics, and quantum information science [16–18]. The charge transport in GNR-based devices can be largely affected by the coupling of electrons to the well-established ribbon vibration modes [1,19,20], e.g., vibrational excitations of GNRs by electrons [17]. Commonly, this process in molecules is treated within the Franck-Condon model [21,22], which assumes instantaneous electronic transitions without changes in nuclear coordinates or momentum [23]. Using scanning tunneling microscopy (STM), vibronic spectroscopy, which records the differential conductance changes during resonant transitions from a molecular ground state to an electronically and vibrationally excited state associated with positive or negative ion resonances [24–33], has been widely adopted to detect the electron-vibration coupling in molecular systems mostly adsorbed on semiconducting or insulating decoupling layers. The decoupling layer plays a critical role, acting as a spacer that extends the lifetime of the transient charged states of molecules [24,28,34–36]. Because of the on-surface synthesis of GNRs mainly on coinage metals, it is almost impossible to probe the vibronic excitations in the as-grown GNRs. Post-transfer of GNRs onto insulating NaCl islands with tip-assisted precise manipulation [2,37,38] and direct growth on semiconducting TiO_2 substrates [39,40] had been achieved. Even so, the understanding of the vibronic states remains elusive in topological GNRs, where the localized vibronic excitations of the topologically protected end states, distinct from previous measurements on trivial molecular frontier orbitals, can promote the intriguing interplay between electrons, vibrons, and topology.

In this Letter, we develop a squeezing-induced spillover approach to on-surface synthesis of second-layer GNRs. By performing low-temperature scanning tunneling microscopy and spectroscopy studies, we observe two vibronic progressions assisted by the negative ion resonance of the empty topological end states in the quasi-freestanding second-layer seven-carbon-wide armchair GNRs (7-AGNRs), which display high tunability of the magnetic end states for exploring the spin-vibronic coupling [41]. Our theoretical simulations that take the Herzberg-Teller contributions [42] into account well reproduce the vibration-assisted wave function variations of the topological end state, suggesting strong vibronic

coupling that goes beyond the conventional Franck-Condon model.

The experiment was performed in a commercial Omicron low-temperature STM system with a base pressure lower than 1×10^{-10} torr. STM imaging and spectroscopy measurements were carried out at 5 K with a well-cleaned polycrystalline tungsten tip. Sample bias voltages were used with respect to the tip. The dI/dV spectra and maps were obtained using a lock-in amplifier with a modulation of 10 mV at 731 Hz. The on-surface synthesis proceeded in a separate preparation chamber on an Au(111) substrate (MaTeck GmbH) [Supplemental Material (SM) [43]].

We first develop an on-surface route to achieving second-layer GNRs by utilizing the squeezing-induced spillover of preformed first-layer GNRs [Fig. 1(a)]. This strategy can be summarized as two steps: (i) an initial synthesis of a GNR sample with coverage slightly lower than one monolayer from precursor P1, and (ii) a second growth on the preformed first-layer GNR sample with precursor P2. Under thermal excitation, some of the first-layer GNRs may be squeezed partially or even fully to the second layer due to the steric hindrance effect induced by the linear P2 products. As a proof of concept, we chose mature molecular precursors, namely, 10,10'-dibromo-9,9'-bianthryl (DBBA) and 6,13-bis(dibromomethylene)-6,13-dihydropentacene (4BrPn) as P1 and P2, to correspondingly synthesize 7-AGNRs [1] [Fig. 1(b)] and polypantacene (PolyPn) chains [44,45] [Fig. 1(c)]. PolyPn polymers first occupy empty sites of the surface with a submonolayer coverage and push the 7-AGNRs closer to each other. With more 4BrPn molecules deposited, second-layer 7-AGNRs and PolyPn polymers can be found [Fig. 1(d) and SM [43]], confirming the squeezing-induced spillover strategy. The enlarged STM image in Fig. 1(e) shows a fully lifted second-layer 7-AGNR with length of about 16 nm going along the first-layer ones near the lower step edge, which may diffuse from the upper terrace. It displays the quasifreestanding signatures with fine textures both in the bulk and ribbon end [37,52] and the enhanced band gap of about 3.13 eV compared with that of about 2.64 eV in the first-layer GNRs (SM [43]), quite close to the *GW* calculated quasiparticle band gap (~3.7 eV) [53]. Similar decoupling behavior is also observed in the second-layer PolyPn chains (SM [43]).

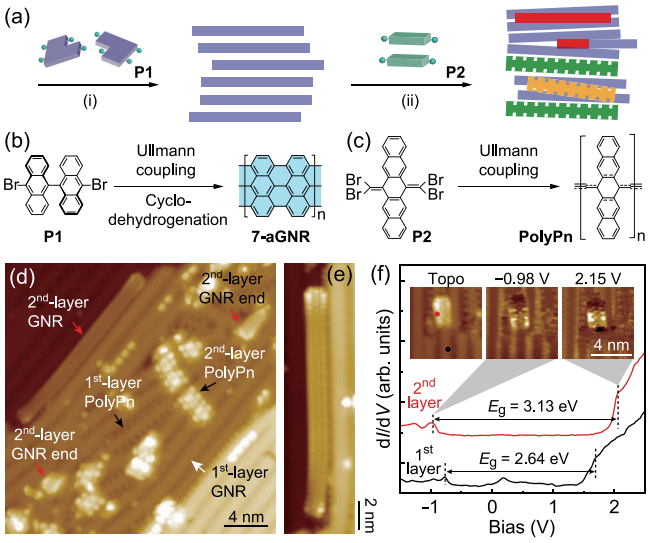

FIG. 1. (a) Schematic illustration of the squeezing-induced spillover strategy for on-surface synthesis of second-layer GNRs. First- and second-layer products from precursors P1 and P2 are denoted by different colors and shapes. (b),(c) Chemical sketches of the on-surface synthesis of the 7-AGNR and PolyPn, respectively. (d) Large-area STM image after successive deposition and annealing of DBBA and 4BrPn ($V_s = 2.0$ V, $I_t = 10$ pA). (e) High-resolution STM image of a second-layer 7-AGNR, located at the lower side of the Au(111) step edge ($V_s = 2.0$ V, $I_t = 10$ pA). (f) dI/dV spectra acquired at edges of the second-layer (red spots) and first-layer 7-AGNR fragments ($V_s = 2.5$ V, $I_t = 10$ pA), as marked in the inset topographic STM image ($V_s = 1.7$ V, $I_t = 10$ pA), together with constant-current dI/dV maps, acquired at energies of valence band maximum (VBM) (−0.98 eV) and conductance band minimum (CBM) (2.15 eV) of the second-layer 7-AGNR.

Notably, while our recent work reported the on-surface synthesis of partially lifted second-layer GNRs through remote-triggered dominolike cyclodehydrogenation and structural-strain engineering of molecular precursors [52], the same strategy failed to form second-layer 7-AGNRs using DBBA [54,55]. Here, the demonstrated strategy should be more general for various precursors to achieve both partially and fully decoupled second-layer structures with nearly intrinsic properties, where the inert and semiconducting first layer acts a self-decoupling layer and still enables detecting the local spins by utilizing the Kondo resonance [52] (SM [43]). A competition between the radiative and nonradiative processes can be derived according to the results in Ref. [35]. This competition should be responsible for either efficient luminescence or efficient vibration-assisted tunneling process for the topological end states of GNRs depending on decoupling layer used, rather than the suggestion of smeared vibronic tunneling by broadening of the ion resonances on NaCl [24,36,37].

In Fig. 2, we focus on the pawlike pristine end of the second-layer 7-AGNR adsorbed at the Au(111) substrate step [Fig. 1(e)], as illustrated in Fig. 2(a). It is supposed to host topologically nontrivial end states [6,37]. Highly resolved dI/dV spectra in Fig. 2(b), recorded at the second-layer end (red and blue), display a pronounced peak at 0.24 V and a series of weak peaks from about 0.4 to 2.3 V, in comparison with the black curve from the nearby bulk (SM [43]). The obviously more asymmetric energies of VBM (−0.53 V) and CBM (2.53 V), compared to those observed in the second-layer GNRs on Au terraces [Fig. 1(f)], suggesting additional hole doping by the step edge. Then the pronounced 0.24 V peak can be reasonably assigned to the elastic negative ion resonance

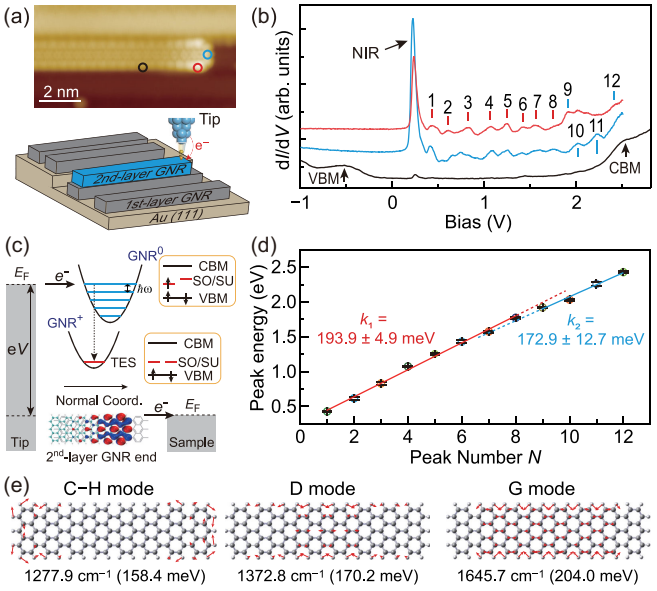

FIG. 2. (a) High-resolution STM image of the second-layer 7-AGNR near the Au step (upper) ($V_s = 2.0$ V, $I_t = 10$ pA) and the schematic diagram (lower). (b) dI/dV spectra acquired at sites marked by corresponding colored spots in (a) ($V_s = 2.5$ V, $I_t = 10$ pA), with the vertical red and blue bars indicating the peaks in two vibronic progressions. (c) Schematic diagram of electron transport through the second-layer GNR topological end state (TES) and the vibrational excitation at a positive sample bias. The occupation change between the GNR^0 and GNR^+ states is also illustrated. (d) Plot of the statistical vibronic peak positions against peak number N (SM [43]), marked with the linear fit slope of each progression, with the statistical significance correspondingly 1.75×10^{-8} and 0.005. (e) Simulated C—H, D, and G vibration modes in a four-DBBA-unit-long 7-AGNR, with the red arrows indicating the normalized atomic displacements.

(NIR) [25–28,30,32,33] when electrons tunnel into the unoccupied topological end state. The additional satellites, above the NIR peak within the bulk band gap, remind us of the vibronic excitations [24–33], as illustrated in Fig. 2(c). Resonant tunneling of an electron into the vibronic states changes the hole-doped GNR^+ ground state to an electronically and vibrationally excited transient GNR^0 state. The residence time of the electron in the GNR^0 is mainly determined by the decoupling from the metallic substrate. Then, the excited GNR^0 can relax through the vibrational mode $\hbar\omega$ [short black arrows in Fig. 2(c)] until returning to the GNR^+ state after the electron leaves the second-layer GNR and tunnels through the first-layer GNR into the Au substrate.

Figure 2(d) plots the statistical vibronic peak positions as function of the peak number N, as marked in Fig. 2(b) and SM [43]. The first eight peaks (1–8) and last four peaks (9–12) separately present the good linear relationship with N, giving slightly different slopes of $k_1 = 193.9 \pm 4.9$ meV and $k_2 = 172.9 \pm 12.7$ meV, respectively. According to the mechanism described in Fig. 2(c), the slopes correspond to energies of vibration modes that participate in the vibronic excitations. Based on recent STM-induced luminescence measurements of the 7-AGNRs on NaCl layers [35], four vibration modes can be dominantly involved in the vibronic excitations at long ribbon ends, which are the infrared active C—H_{IR} mode (677 cm^{-1}) and three Raman active modes, i.e., the C—H, D, and G modes, also shown in Fig. 2(e). Typically, the C—H mode at 1277.9 cm^{-1} corresponds to in-plane C—H bond bending at GNR edges at the end. The D and G modes, at 1372.8 and 1645.7 cm^{-1}, respectively, are associated with E_{2g} and A_{1g} deformations of carbon rings, commonly seen in sp^2-carbon materials [56]. While the C—H_{IR} mode has a low energy of about 84 meV, and may be safely excluded, the other three modes all fall in the reasonable energy range and can contribute to the observed vibronic progressions.

The contribution of different vibration modes to vibronic states can be distinguished by highly spatially resolved dI/dV maps, since vibrations with different patterns may significantly modify the topological end state wave function [29]. The dI/dV map acquired at the NIR energy [Fig. 3(a)] can well resemble the simulated wave functions of the topological end states [Fig. 3(b)]. The simulation-revealed gap between the spin-polarized singly occupied and singly unoccupied molecular orbitals (SOMO and SUMO) is absent in our experiment, which can be attributed to the greatly suppressed Coulomb interactions due to the strong hole doping effect [57]. The constant-height dI/dV maps acquired at peaks of the first [Fig. 3(c)] and second [Fig. 3(f)] vibronic progressions show quite similar features for those from the same progressions, but apparently different between the two progressions. Typically, the dI/dV maps in Fig. 3(c) display similar pawlike patterns to that of the NIR [Fig. 3(a)], with three bright spots at the short zigzag end, while those features are missing in Fig. 3(f). To better present the difference, we subtract each dI/dV map in Fig. 3(c) or 3(f) from the map in Fig. 3(a) and obtain the averaged figure, shown in Fig. 3(d) or 3(g) (for details, see SM [43]). It may be reconciled in the frame of vibronic coupling theory [23]. Indeed, according to the purely Franck-Condon principle, one would expect that all the maps taken at energies of the vibronic peaks should faithfully duplicate the one of the NIR peak since they stem from the same electronic transition, with their relative intensities determined by vibrational wave function overlap integrals. Thus, while the first progression can be simply put into the Franck-Condon regime, the distinct inelastic vibration-assisted contribution for the second progression shows evidence of the vibronic coupling that goes beyond the conventional Franck-Condon model.

To simulate these contributions, we take the Herzberg-Teller expansion [42,58] into account, which treats the vibration as a perturbation for the wave function of the vibrationally excited molecule [29]. Figure 3(e) presents

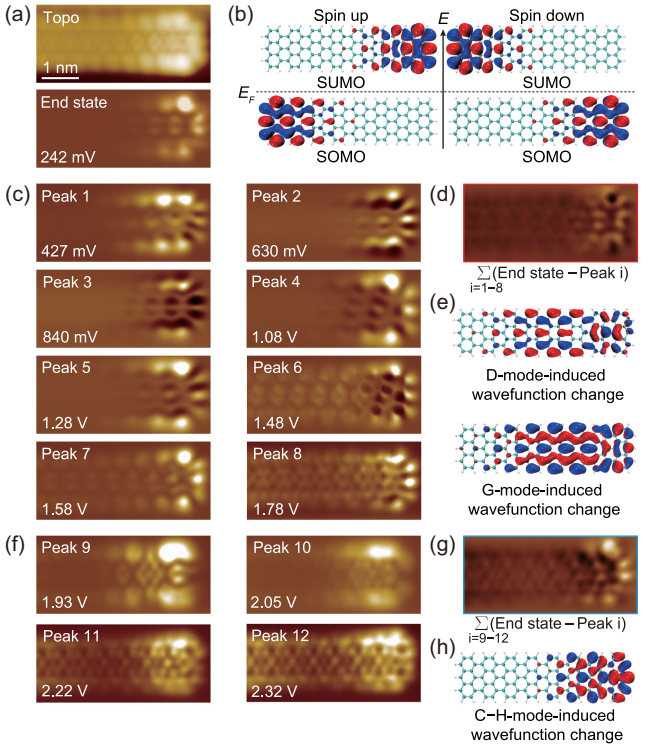

FIG. 3. (a) Close-up STM image of the second-layer 7-AGNR end (upper) ($V_s = 2.0$ V, $I_t = 10$ pA) and the constant-height dI/dV map acquired at the NIR peak energy of 242 mV (lower). (b) Simulated wave functions of the spin-polarized end states of a four-unit-long 7-AGNR, with blue and red colors indicating different signs of the wave functions. (c),(f) Constant-height dI/dV maps acquired at energies of the inelastic peaks 1–8 (c) and peaks 9–12 (f). (d) Average difference between dI/dV maps in (a) and (c), and (g) between those in (a) and (f). (e), (h) Simulated vibration-induced changes of the end state wave function considering the contribution of the D and G modes (e) and the C—H mode (h), respectively.

the simulated wave function changes of the topological end state induced by the D and G modes, while Fig. 3(h) is the case of the C—H mode (SM [43]). Clear resemblance can be found between the C—H-mode-assisted wave function change [Fig. 3(h)] and Fig. 3(g), revealing the C—H-mode-assisted tunneling of the second vibronic progression (peaks 9–12). In addition, the vibration energy (158.4 meV) of the C—H mode [Fig. 2(e)] is also comparable with the experimentally extracted value (172.9 meV) [Fig. 2(d)]. Additional electron tunneling through the CBM lower edge around 2 V can further excite the localized C—H mode to appear dominantly above the 9 peak, while our simulation suggests a relatively weak contribution of the C—H mode-induced CBM wave function change (SM [43]). Based on a different transition between the ground neutral state and a neutral excited state [35], the previous STM-induced luminescence measurements observed vibronic excitations associated with the topologically localized excitons in the NaCl-decoupled 7-AGNRs, where the nonadiabatic coupling was promoted by the C—H_{IR} mode. For the first vibronic progression (peaks 1–8), both the simulated wave function changes induced by the D and G modes show weaker intensities at the ribbon end, significantly different from that induced by the C—H mode, but in accordance with the feature in Fig. 3(d). Considering the other fact that their vibration energies of 170.2 and 204.0 meV are also close to the deduced value of 193.9 meV for the first progression, we believe that both of them can contribute to the vibrational excitations. These results suggest a different vibronic picture that the topology of the GNRs and the spatial distribution of vibrational modes should play a role in determining the pure vibronic or vibration-assisted tunneling. Because of the broken translational symmetry at terminals of the 7-AGNR, topological boundary states and localized vibration modes, here the C—H mode, coreside at the ribbon ends, resulting in vibration-assisted tunneling beyond the conventional Franck-Condon model. This behavior is reconciled with the nontrivially topological nature of the 7-AGNR, which may be extended to other decoupled low-dimensional topological materials with inherently localized topological states and vibration modes at the same boundaries.

Another advantage of the fully lifted second-layer GNR is tunability of the local chemical potential by surrounding environments [52]. As shown in Figs. 4(a) and 4(b), the first five dI/dV spectra of the 19 spectra taken along the ribbon edge from the pristine End1 to contaminated End2 show the

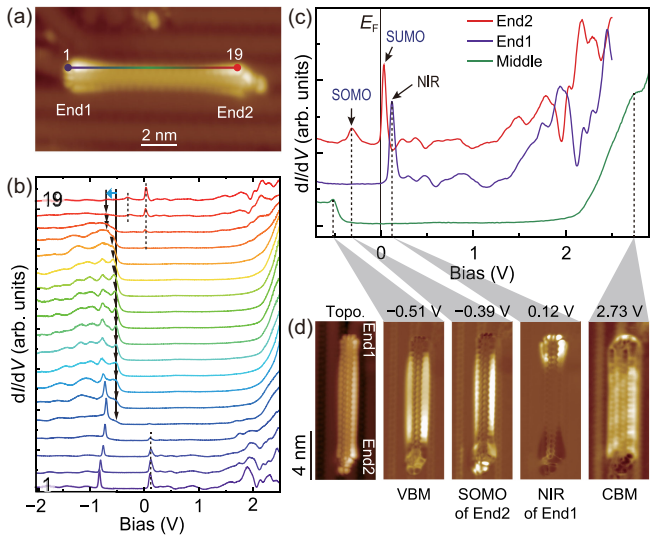

FIG. 4. (a) High-resolution STM image of another second-layer 7-AGNR ($V_s = 2.0$ V, $I_t = 10$ pA). (b) Nineteen dI/dV spectra collected with equal spacing from End1 (left) to End2 (right) along the color-coded line in (a) ($V_s = 2.5$ V, $I_t = 10$ pA). (c) dI/dV spectra taken at End1, End2, and the middle site along the edges ($V_s = 2.5$ V, $I_t = 10$ pA). (d) Constant-current topographic image ($V_s = -0.51$ V, $I_t = 10$ pA) and dI/dV maps obtained at energies as marked.

pronounced NIR peak at 0.12 V near End1, similar to that observed in Fig. 2(b). A different sharp peak with clearly site-dependent peak positions at about −0.70 to −0.83 V, corresponding to the ringlike conductance enhancement in the dI/dV maps (SM [43]), is the charging state by adding one electron in the empty topological end state due to the tip-induced local gating effect [50–52]. Similar charging state is also observed for the end state at 0.24 V in Fig. 2(a) (SM [43]), but with an approximately doubled energy. These results give a nearly constant voltage drop with a ratio of about 0.16 across the lower GNR layer, by using the formula $E_{\mathrm{TES}}/(E^{-}-E_{\mathrm{TES}})$, where E_{TES} and E^{-} are energies of the topological end states and the charging peaks, respectively. This behavior can be ascribed to the tip-induced ionization mechanism [51], also as illustrated in SM [43]. These results, from a different aspect, again confirm the quasifreestanding nature of the second-layer GNRs.

When approaching End2, the VBM shifts from −0.53 down to −0.69 eV by 0.16 eV (blue arrow), due to the local chemical potential tuned by the nearby physically adsorbed contamination, as further suggested by tip manipulation (SM [43]). At End2, we observe two distinct peaks at −0.30 and 0.03 eV, respectively, corresponding to the splitting SOMO and SUMO [Fig. 3(b) and SM [43]], resulting from the enhanced Coulomb interaction after the downshift of the empty topological end state to the Fermi level. As shown in Fig. 4(c), spectra taken at two ends display almost identical vibronic states at positive biases, except for the energy shift (SM [43]). The above assignments can be further confirmed by the dI/dV maps acquired at energies corresponding to the VBM (−0.51 eV) and CBM (2.73 eV) with dominant intensities at the ribbon bulk, and the end states of End1 (0.12 eV) and End2 (−0.39 eV). Notably, since the SUMO is spin-polarized at End2 [Fig. 3(b)], it may suggest the possibility of exploring the spin-vibronic coupling [41,59] in this system.

In conclusion, we demonstrate an effective squeezing-induced spillover strategy for the on-surface synthesis of second-layer GNRs. Two vibronic progressions with slightly different spacings are observed at the quasifreestanding second-layer 7-AGNR ends, benefiting from the resonant vibrational excitations assisted by the NIR of the empty topological end states. Based on atomically resolved vibronic spectroscopic maps, we unveil distinct vibration-induced wave function changes to the topological end states, which are well captured by our theoretical simulations by taking into account the Herzberg-Teller contributions, providing direct evidence of vibronic coupling that moves beyond the Franck-Condon principle. Our thorough exposition of the interplay between electrons, vibrons, and topology at the atomic scale provides valuable experimental benchmarks for future research in the field of topological materials.

This work was supported by the Innovation Program for Quantum Science and Technology (No. 2021ZD0303302), the National Natural Science Foundation of China (No. 22002149, No. 12074359, and No. 12304235), the Chinese Academy of Sciences (No. XDB36020200), the CAS Project for Young Scientists in Basic Research (YSBR-054), the Anhui Initiative in Quantum Information Technologies (No. AHY090000), the New Cornerstone Science Foundation, and the Fundamental Research Funds for the Central Universities.

*Contact author: cxma85@ustc.edu.cn
†Contact author: bwang@ustc.edu.cn

[1] J. Cai, P. Ruffieux, R. Jaafar, M. Bieri, T. Braun, S. Blankenburg, M. Muoth, A. P. Seitsonen, M. Saleh, X. Feng, K. Müllen, and R. Fasel, Nature (London) **466**, 470 (2010).
[2] P. Ruffieux, S. Wang, B. Yang, C. Sanchez-Sanchez, J. Liu, T. Dienel, L. Talirz, P. Shinde, C. A. Pignedoli, D. Passerone, T. Dumslaff, X. Feng, K. Müllen, and R. Fasel, Nature (London) **531**, 489 (2016).
[3] S. Clair and D. G. de Oteyza, Chem. Rev. **119**, 4717 (2019).
[4] R. S. K. Houtsma, J. de la Rie, and M. Stöhr, Chem. Soc. Rev. **50**, 6541 (2021).
[5] Y. Gu, Z. Qiu, and K. Müllen, J. Am. Chem. Soc. **144**, 11499 (2022).
[6] T. Cao, F. Zhao, and S. G. Louie, Phys. Rev. Lett. **119**, 076401 (2017).
[7] O. Gröning, S. Wang, X. Yao, C. A. Pignedoli, G. Borin Barin, C. Daniels, A. Cupo, V. Meunier, X. Feng, A. Narita, K. Müllen, P. Ruffieux, and R. Fasel, Nature (London) **560**, 209 (2018).
[8] D. J. Rizzo, G. Veber, T. Cao, C. Bronner, T. Chen, F. Zhao, H. Rodriguez, S. G. Louie, M. F. Crommie, and F. R. Fischer, Nature (London) **560**, 204 (2018).
[9] N. V. Tepliakov, J. Lischner, E. Kaxiras, A. A. Mostofi, and M. Pizzochero, Phys. Rev. Lett. **130**, 026401 (2023).
[10] F. Zhao, T. Cao, and S. G. Louie, Phys. Rev. Lett. **127**, 166401 (2021).
[11] F. M. Arnold, T.-J. Liu, A. Kuc, and T. Heine, Phys. Rev. Lett. **129**, 216401 (2022).
[12] S. Song, J. Su, M. Telychko, J. Li, G. Li, Y. Li, C. Su, J. Wu, and J. Lu, Chem. Soc. Rev. **50**, 3238 (2021).
[13] F. Lombardi, A. Lodi, J. Ma, J. Liu, M. Slota, A. Narita, W. K. Myers, K. Müllen, X. Feng, and L. Bogani, Science **366**, 1107 (2019).
[14] S. Mishra, D. Beyer, K. Eimre, S. Kezilebieke, R. Berger, O. Gröning, C. A. Pignedoli, K. Müllen, P. Liljeroth, P. Ruffieux, X. Feng, and R. Fasel, Nat. Nanotechnol. **15**, 22 (2020).
[15] R. E. Blackwell, F. Zhao, E. Brooks, J. Zhu, I. Piskun, S. Wang, A. Delgado, Y.-L. Lee, S. G. Louie, and F. R. Fischer, Nature (London) **600**, 647 (2021).
[16] H. Wang, H. S. Wang, C. Ma, L. Chen, C. Jiang, C. Chen, X. Xie, A.-P. Li, and X. Wang, Nat. Rev. Phys. **3**, 791 (2021).
[17] J. Zhang, L. Qian, G. B. Barin, A. H. S. Daaoub, P. Chen, K. Müllen, S. Sangtarash, P. Ruffieux, R. Fasel, H. Sadeghi, J.

Zhang, M. Calame, and M. L. Perrin, Nat. Electron. **6**, 572 (2023).
[18] V. Saraswat, R. M. Jacobberger, and M. S. Arnold, ACS Nano **15**, 3674 (2021).
[19] C. Ma, L. Liang, Z. Xiao, A. A. Puretzky, K. Hong, W. Lu, V. Meunier, J. Bernholc, and A.-P. Li, Nano Lett. **17**, 6241 (2017).
[20] J. Overbeck, G. B. Barin, C. Daniels, M. L. Perrin, O. Braun, Q. Sun, R. Darawish, M. De Luca, X.-Y. Wang, T. Dumslaff, A. Narita, K. Müllen, P. Ruffieux, V. Meunier, R. Fasel, and M. Calame, ACS Nano **13**, 13083 (2019).
[21] E. Condon, Phys. Rev. **28**, 1182 (1926).
[22] J. Franck and E. G. Dymond, Trans. Faraday Soc. **21**, 536 (1926).
[23] G. Fisher, *Vibronic Coupling: The Interaction between the Electronic and Nuclear Motions* (Academic Press, London, 1984).
[24] N. Krane, C. Lotze, G. Reecht, L. Zhang, A. L. Briseno, and K. J. Franke, ACS Nano **12**, 11698 (2018).
[25] N. Liu, N. A. Pradhan, and W. Ho, J. Chem. Phys. **120**, 11371 (2004).
[26] N. Ogawa, G. Mikaelian, and W. Ho, Phys. Rev. Lett. **98**, 166103 (2007).
[27] N. Pavliček, I. Swart, J. Niedenführ, G. Meyer, and J. Repp, Phys. Rev. Lett. **110**, 136101 (2013).
[28] X. H. Qiu, G. V. Nazin, and W. Ho, Phys. Rev. Lett. **92**, 206102 (2004).
[29] G. Reecht, N. Krane, C. Lotze, L. Zhang, A. L. Briseno, and K. J. Franke, Phys. Rev. Lett. **124**, 116804 (2020).
[30] F. Schwarz, Y. F. Wang, W. A. Hofer, R. Berndt, E. Runge, and J. Kröger, J. Phys. Chem. C **119**, 15716 (2015).
[31] K. J. Franke and J. I. Pascual, J. Phys. Condens. Matter **24**, 394002 (2012).
[32] F. Matino, G. Schull, F. Köhler, S. Gabutti, M. Mayor, and R. Berndt, Proc. Natl. Acad. Sci. U.S.A. **108**, 961 (2011).
[33] G. V. Nazin, S. W. Wu, and W. Ho, Proc. Natl. Acad. Sci. U.S.A. **102**, 8832 (2005).
[34] X. H. Qiu, G. V. Nazin, and W. Ho, Science **299**, 542 (2003).
[35] S. Jiang, T. Neuman, A. Boeglin, F. Scheurer, and G. Schull, Science **379**, 1049 (2023).
[36] J. Repp, G. Meyer, S. Paavilainen, F. E. Olsson, and M. Persson, Phys. Rev. Lett. **95**, 225503 (2005).
[37] S. Wang, L. Talirz, C. A. Pignedoli, X. Feng, K. Müllen, R. Fasel, and P. Ruffieux, Nat. Commun. **7**, 11507 (2016).
[38] P. H. Jacobse, M. J. J. Mangnus, S. J. M. Zevenhuizen, and I. Swart, ACS Nano **12**, 7048 (2018).
[39] M. Kolmer, A. K. Steiner, I. Izydorczyk, W. Ko, M. Engelund, M. Szymonski, A.-P. Li, and K. Amsharov, Science **369**, 571 (2020).
[40] R. Zuzak, J. Castro-Esteban, M. Engelund, D. Pérez, D. Peña, and S. Godlewski, ACS Nano **17**, 2580 (2023).
[41] S. Rafiq, N. P. Weingartz, S. Kromer, F. N. Castellano, and L. X. Chen, Nature (London) **620**, 776 (2023).
[42] T. Azumi and K. Matsuzaki, Photochem. Photobiol. **25**, 315 (1977).
[43] See Supplemental Material at http://link.aps.org/supplemental/10.1103/PhysRevLett.133.036401 for details on the sample preparation and characterization, theoretical calculations, additional data, and analysis of the first and second-layer PolyPn chains and GNRs, which includes Refs. [44–51].
[44] B. Cirera, A. Sánchez-Grande, B. de la Torre, J. Santos, S. Edalatmanesh, E. Rodríguez-Sánchez, K. Lauwaet, B. Mallada, R. Zbořil, R. Miranda, O. Grüning, P. Jelínek, N. Martín, and D. Ecija, Nat. Nanotechnol. **15**, 437 (2020).
[45] H. González-Herrero, J. I. Mendieta-Moreno, S. Edalatmanesh, J. Santos, N. Martín, D. Écija, B. de la Torre, and P. Jelinek, Adv. Mater. **33**, e2104495 (2021).
[46] M. J. Frisch *et al.*, Gaussian 16 Rev. A.03 (Gaussian, Inc., Wallingford CT, 2016), https://gaussian.com/citation_a03/.
[47] T. Lu and F. Chen, J. Comput. Chem. **33**, 580 (2011).
[48] J. Tersoff and D. R. Hamann, Phys. Rev. Lett. **50**, 1998 (1983).
[49] P. Ruffieux, J. Cai, N. C. Plumb, L. Patthey, D. Prezzi, A. Ferretti, E. Molinari, X. Feng, K. Müllen, C. A. Pignedoli, and R. Fasel, ACS Nano **6**, 6930 (2012).
[50] N. A. Pradhan, N. Liu, C. Silien, and W. Ho, Phys. Rev. Lett. **94**, 076801 (2005).
[51] V. W. Brar, R. Decker, H.-M. Solowan, Y. Wang, L. Maserati, K. T. Chan, H. Lee, Ç. O. Girit, A. Zettl, S. G. Louie, M. L. Cohen, and M. F. Crommie, Nat. Phys. **7**, 43 (2011).
[52] C. Ma, J. Wang, H. Ma, R. Yin, X.-J. Zhao, H. Du, X. Meng, Y. Ke, W. Hu, B. Li, S. Tan, Y.-Z. Tan, J. Yang, and B. Wang, J. Am. Chem. Soc. **145**, 10126 (2023).
[53] L. Yang, C.-H. Park, Y.-W. Son, M. L. Cohen, and S. G. Louie, Phys. Rev. Lett. **99**, 186801 (2007).
[54] C. Ma, Z. Xiao, H. Zhang, L. Liang, J. Huang, W. Lu, B. G. Sumpter, K. Hong, J. Bernholc, and A.-P. Li, Nat. Commun. **8**, 14815 (2017).
[55] Z. Mutlu, J. P. Llinas, P. H. Jacobse, I. Piskun, R. Blackwell, M. F. Crommie, F. R. Fischer, and J. Bokor, ACS Nano **15**, 2635 (2021).
[56] A. C. Ferrari and D. M. Basko, Nat. Nanotechnol. **8**, 235 (2013).
[57] M. Ijäs, M. Ervasti, A. Uppstu, P. Liljeroth, J. van der Lit, I. Swart, and A. Harju, Phys. Rev. B **88**, 075429 (2013).
[58] F.-F. Kong, X.-J. Tian, Y. Zhang, Y.-J. Yu, S.-H. Jing, Y. Zhang, G.-J. Tian, Y. Luo, J.-L. Yang, Z.-C. Dong, and J. G. Hou, Nat. Commun. **12**, 1280 (2021).
[59] M. K. Etherington, J. Gibson, H. F. Higginbotham, T. J. Penfold, and A. P. Monkman, Nat. Commun. **7**, 13680 (2016).